

Monte Carlo Radiative Transfer

rrti

May 22, 2014

Abstract

Monte Carlo methods for solving the radiative transfer problem have proven very popular for their conceptual simplicity and accuracy. In this article we investigate their ability to simulate a stellar system blocked from direct view by both homogeneous and heterogeneous clouds of dust. A computer program is presented that calculates the transfer of energy through these types of distributions using a Monte Carlo transfer code and outputs a visualization of the system as it might appear when observed with a modern high-resolution telescope. Results are compared to the analytical solution for a semi-infinite plane-parallel slab; extensions to the program are also discussed.

1 Introduction

Radiative Transfer [2] is the physical process by which energy (in the form of electromagnetic radiation) is transferred through a medium, which involves absorption, emission, and scattering interactions. These interactions are described mathematically by the equations of radiative transfer, and are of importance in formalisms as diverse as astrophysics and computer graphics. However, for all but the simplest cases, analytical solutions to these equations do not exist and have to be approximated numerically. The Monte Carlo [4] class of computational algorithms is perhaps the most widely used approximation technique. In Monte Carlo radiative transfer, photons are released from an emission source and tracked as they probabilistically interact with matter

in a simulated medium such as gas or dust. This conceptually somewhat trivial model nevertheless allows fully arbitrary distributions of the interacting material to be simulated, which is of vital importance for eg. the study of (images of) astronomical objects like spiral galaxies [3] possessing many non-uniform characteristics. The basic components of this model are:

- Scattering: a photon's trajectory is altered according to a given probability distribution, which depends on the local properties of the medium the photon is travelling through
- Absorption: the energy quantum represented by a photon is taken up by the matter and converted into another form, eg. heat
- Re-emission: some of the energy added to the material via the absorption of photons is released in the form of new photon packets

When absorption and re-emission happen in sequence, the effect is that of a scattering event. However, absorption followed by re-emission can result in significant changes in photon energy, which is not true for genuine scattering. Since ensuring the model's physical correctness is much harder when re-emission is considered, we limit its scope to absorption and scattering only. As an example, figure 1 shows the diffusion of visible light from stars in a nebula caused by these interactions.

2 Theoretical Background

We first give a brief overview of the concepts in radiative transfer that are necessary to understand the

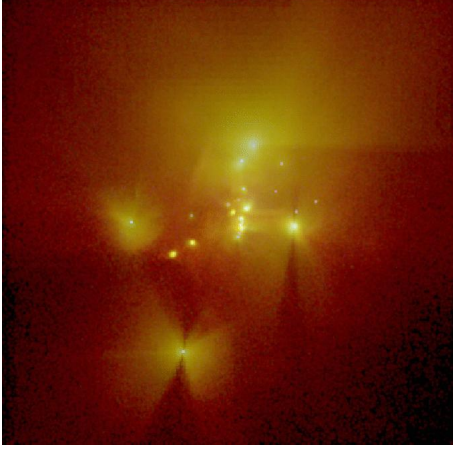


Figure 1: Radiative Transfer in a stellar nebula (image from the TORUS RT simulation developed at the University of Exeter).

general workings of the Monte Carlo simulation. The quantity most directly of interest is the specific intensity I_v of the radiation field, defined as the amount of radiant energy δE_v passing through a unit surface area δA at an angle θ to the area surface normal within a solid angle¹ $\delta\Omega$ in a frequency range δv in an interval of time δt , or

$$I_v = \frac{\delta E_v}{\cos \theta \delta A \delta t \delta v \delta \Omega} \quad (1)$$

[ergs cm⁻² s⁻¹ Hz⁻¹ sr⁻¹] where each photon represents a quantum of energy δE_v , and the total energy is split equally among all the photons tracked². This can be visualized as a cone of radiation emanating from δA , shown in figure 2. The *rate* of energy flow across a unit area δA per unit time per unit frequency

¹The area Ω of a surface when projected onto a unit sphere, expressed in steradians *sr* (the 2D analogue of radians).

²In the real world a photon's energy is directly proportional to its frequency, but we assume all photons are born – and remain – equally energetic.

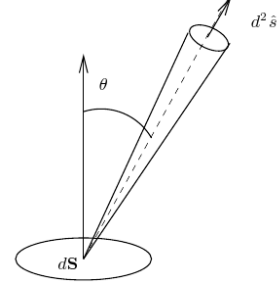


Figure 2: The Specific Intensity. dS is the infinitesimal surface area patch through which an amount of energy δE flows at an angle θ to the surface normal (image from [7]).

interval is known as the flux, and is defined as

$$F_v = \int I_v \cos \theta \delta \Omega \quad (2)$$

or

$$F_v = \int \frac{\delta E_v}{\delta A \delta t \delta v} \quad (3)$$

making its unit of measurement [ergs cm⁻² s⁻¹ Hz⁻¹] explicit.

Three important properties closely tied to the intensity are the so-called *intensity moments*, which together provide an indication of the medium's thermodynamical activity. The trinity is comprised of the mean intensity J , the mean flux H , and the mean radiation pressure K :

$$J = \frac{1}{4\pi} \int I \delta \Omega \quad (4)$$

$$H = \frac{1}{4\pi} \int I \cos(\theta) \delta \Omega \quad (5)$$

$$K = \frac{1}{4\pi} \int I \cos(\theta)^2 \delta \Omega \quad (6)$$

We will refer back to these moments in section 3 in the context of model validation.

The difference between the number of incoming and outgoing photons at any point in the field determined by the scattering and absorption cross-sections of the particles that make up the medium. More precisely, a particle's cross-section σ tells us how much energy that particle removes along the direction of travel per second per frequency per solid angle, so that we can introduce an intermediate quantity

$$E_r = I_v \sigma \quad (7)$$

which is the energy removed *per second per frequency*.

Now suppose the medium is homogeneous and has particle density (concentration) n . The number of photons removed per second along a line of length δl is then $E_r n \delta l$, so the intensity differential equation satisfies

$$\delta I_v = -E_r n \delta l = -I_v \sigma n \delta l \quad (8)$$

which has the closed-form solution

$$I_v(l) = I_v(0)e^{-n\sigma l} \quad (9)$$

meaning the amount of photons that undergo a scattering or absorption event per unit length is $n\sigma$. This number is related to the medium's opacity coefficient κ and mass density ρ as follows

$$n\sigma = \rho\kappa \quad (10)$$

and is the reciprocal of the photon mean free path $\frac{1}{n\sigma}$ (the average distance between interactions). The *probability* of an interaction between a photon and a particle over a length δl is therefore simply $n\sigma\delta l$. If we next assume the distance traversed by the photon until it interacts is L and discretize this into N equally long segments, we obtain the medium's *optical depth* τ from the probability of a photon covering this distance unhindered, or

$$P(L) = (1 - n\sigma \frac{L}{N})^N = e^{-n\sigma L} = e^{-\tau} \quad (11)$$

where $\tau = n\sigma L = \int_0^L n\sigma dl$ can be regarded as the number of mean free paths distributed over L .

The optical depth is a generally useful metric since it combines the medium's defining characteristics (opacity and density).

Once a photon has travelled L , it will either scatter or be absorbed. The "selection" of one of these two fates is governed by the *albedo*, which is defined as the normalized scattering probability

$$a = \frac{n_s \sigma_s}{n_s \sigma_s + n_a \sigma_a} \quad (12)$$

and allows us to simulate any type of medium by letting a range from 1 (fully scattering) to 0 (fully absorbing). If a photon is scattered, then its new direction is derived from the *phase function* $P(\cos \chi)$, which assigns to each angular difference $\mu = \cos \chi$ a probability such that $\int_{-1}^1 P(\mu) d\mu = 1$. The phase function is determined by the type of matter of which the medium is composed, and is often taken to be isotropic ($P(\cos \chi) = \frac{1}{2}$).

3 Transfer Model

3.1 The Plane-Parallel Slab

In his seminal treatise on radiative transfer, Chandrasekhar [2] presented a solution to the question of how the intensity and polarization of the radiation escaping from a homogeneous, isotropic-scattering, semi-infinite medium are related to the angles at which photons are scattered within it. Such a medium can be thought of as an axis-aligned slab of material that is infinite in two dimensions and placed between the radiation source (eg. a star) and the observer. In the z -dimension the slab extends only along the interval $[0, z_{\max}]$, restricting its total vertical optical depth to $\tau_{\max} = n\sigma z_{\max}$. Figure 3 depicts the situation schematically. Taking after [1] this scenario is easily reproduced in a computer program, allowing us to verify the theory discussed so far. Photons are generated at the source position (x_0, y_0, z_0) and given a direction in spherical coordinates (zenith, azimuth) = (θ, ϕ) toward the rear side of the slab. Note that the directions should be chosen in such a manner that the emission

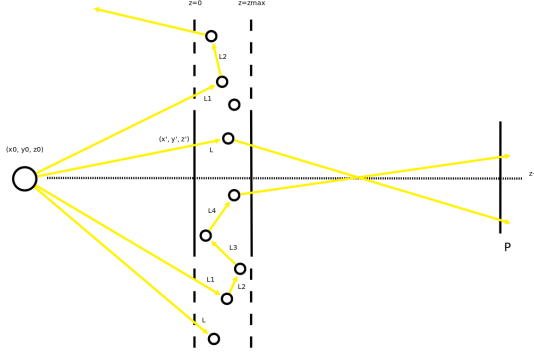


Figure 3: The Semi-Infinite Slab. Particulate matter is not modelled, interactions occur probabilistically (which makes the model an advanced random walk).

flux is isotropic as well. This is achieved by drawing two uniformly distributed random numbers ξ_0 and ξ_1 for every photon and setting $\mu = \cos \theta = \sqrt{\xi_0}$ and $\phi = 2\pi\xi_1$. Once a photon enters the slab at (x', y', z') , we know it will move a distance $L = \frac{\tau z_{\max}}{\tau_{\max}}$ until the first interaction event occurs. To find L , we just invert (11) and randomly sample the non-interaction length (optical depth)³ by letting $\tau = -\log \xi$. We then update the photon's position along its direction of travel, which in Cartesian coordinates is $(dx, dy, dz) = (\sin \theta \cos \phi, \sin \theta \sin \phi, \cos \theta)$, to the point of interaction at $(x' + Ldx, y' + Ldy, z' + Ldz)$. Now the photon either escapes the slab ($z < 0$ or $z > z_{\max}$) or scatters; in the latter case the process is repeated after choosing a new direction ($\mu = \cos \theta = 2\xi_0 - 1, \phi = 2\pi\xi_1$) which guarantees all 4π steradians are sampled uniformly. In pseudocode, this mechanism can be summarized in a few lines:

```
while i < number of photons to generate
  p <-- new photon
  while p inside slab
    sample non-interaction length L
```

³When simulating non-homogeneous media another approach is needed, as section 3.3 explains.

```
    update p's position with L
    if random(0, 1) < albedo
      scatter p's direction
    else
      absorb p

  project p onto image plane
  inc i
```

Since the empty space between the photon source and the slab does not affect the photon paths beyond their initial spread, it is convenient to let $(x_0, y_0, z_0) = (0, 0, 0)$.

3.2 Output and Validation

Recall that we primarily seek to calculate the slab's emergent intensity and flux distribution. To get insight into these distributions we need a method to accumulate or “bin” our photon samples as they exit the dust medium, and preferably a visualization routine. One natural choice for the former is to use m unique $(\mu = \cos \theta, \phi)$ bins. This way each bin corresponds to an equal solid angle, but we require potentially quite many to capture the full range of angle variations. For our simplified slab system however, we can exploit axial symmetry and omit the ϕ -bins. After running the model and filling the bins, we then have a per-bin estimate of the outgoing energy $\frac{\delta E_i}{\delta E} = \frac{N_i}{N_t}$ where N_i is the number of photons that hit bin i and N_t the total number of photons spawned at the source. The intensity in bin i directly follows from (1); $I_v = \frac{N_i}{N_t} \frac{F_v}{\mu \delta \Omega}$ where F_v is equal to $\frac{\delta E}{\delta A}$.

However, because we model the transfer of radiation as a stochastic process, the binned output values will be subject to sampling errors. Now since the number of photons hitting bin i is Poisson-distributed, the error σ_{E_i} will behave according to $\frac{E_i}{\sqrt{N_i}} = \frac{N_i/N_t}{\sqrt{N_i}}$. This demonstrates the main weakness of Monte Carlo simulations: the demand

for a large amount of statistical data, in our case photon trajectories, and lack of explicit error control. Luckily the nature of the radiative transfer model (each photon can be independently traced) permits very easy parallelization, as described in section 4. By way of comparison, the two graphs in figure 4 illustrate the error for $N_t = 10^5$ and $N_t = 10^6$. Visualizing the system is accomplished with the

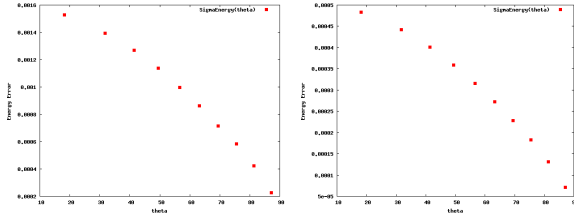


Figure 4: Error in the energy received per θ -bin. We have no control over how much energy $E_i = \frac{N_i}{N_t}$ reaches bin i , but this ratio should stabilize as $N_t \rightarrow \infty$ (at which point σ_{E_i} should start decreasing monotonically). Despite N_t being an order of magnitude larger for the right-side graph, the reduction in error is only on the scale of the square root of this difference.

help of some Euclidean geometry. We know each surviving photon's last position and direction of egress, and the image-plane equation of the observer (whom we may in fact place at any arbitrary position $\vec{V} = (x_O, y_O, z_O)$ in front of the slab; the viewing direction is then just $\frac{-\vec{V}}{\|\vec{V}\|}$ and the plane normal its negation, ie. $\frac{\vec{V}}{\|\vec{V}\|}$). By intersecting the photon ray segments with the image plane and turning these intersection points into pixel coordinates⁴, we build up a snapshot of the emergent energy reaching the observer, much like an actual telescope pointed at an obscured star would. Figure 5 gives an impression of the resulting images. Validation of the slab model

⁴This differs slightly from the conventional image generation method, where only photons parallel to the viewing direction are projected.

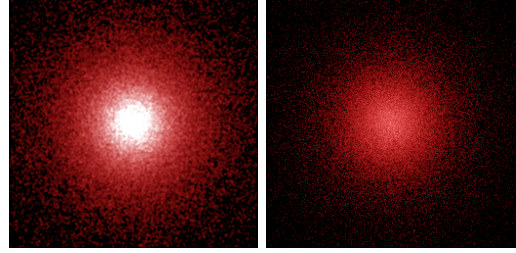


Figure 5: The observed energy. The image on the left appears brighter because each intersection was interpreted as affecting a weighted 3x3 neighbourhood in an effort to increase visual quality while leaving the number of photons constant. Whiter colors represent greater energy levels, wavelengths are not tracked.

consists of two steps. We plot the emergent total intensity I as a function of the θ exit angle and compare this to Chandrasekhar's analytical result for isotropic scattering. We also calculate the intensity moments J , H , and K as a function of optical depth by dividing the slab into k parallel slices and keeping track of the photon transitions between them. In the discrete world, the formulae become⁵:

$$J = \frac{F_v}{4\pi N_t} \sum_i \frac{1}{|\mu_i|}$$

$$H = \frac{F_v}{4\pi N_t} \sum_i \frac{\mu_i}{|\mu_i|}$$

$$K = \frac{F_v}{4\pi N_t} \sum_i \frac{\mu_i^2}{|\mu_i|}$$

Figure 6 shows the simulation's intensity outputs, figure 7 the moments. Both were produced in one run with an identical set of parameters.

⁵The derivation involves substituting the specific intensity contribution $\Delta I = \frac{F_v}{|\mu| N_t \delta\Omega}$ from a single photon into the expressions and then converting the integrals into summations.

Here the H moment should be constant because each photon entering a slice will eventually leave it again, while K should be decreasing with *smaller* optical depth because the net photon motion tends towards the z_{\max} side (which is the outer layer of the scattering atmosphere). This means that the simulation correctly recreates the radiation pressure gradient predicted by radiative transfer theory (as well as matching [1]). We refer the reader to [2] to confirm that the emergent intensities are also in agreement with the theory.

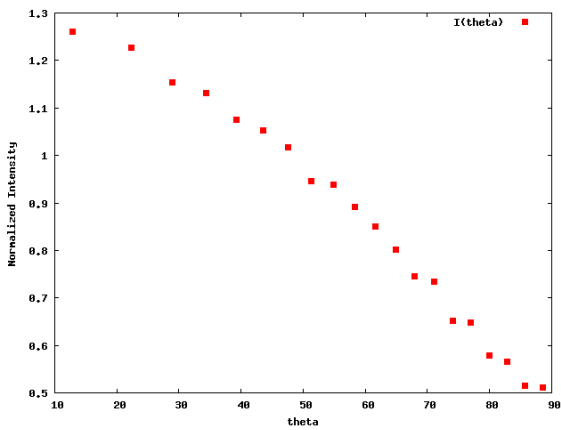


Figure 6: Normalized intensities per θ -bin; parameters $\tau_{\max} = 10, z_{\max} = 1.0, a = 1, m = 20, N_t = 10^5$. At larger angles, fewer photons emerge from the slab.

3.3 Extensions

The isotropic scattering assumed until now is not a realistic approximation of many real astrophysical systems, nor is the homogeneous plane-parallel slab environment. Regarding scattering interactions, stellar dust tends to reflect electromagnetic radiation at preferential angles depending on the size, shape, cross-section, refractive index, and orientation of the particles. This *anisotropy* has to be accounted for if the simulation is to be of any practical use. In

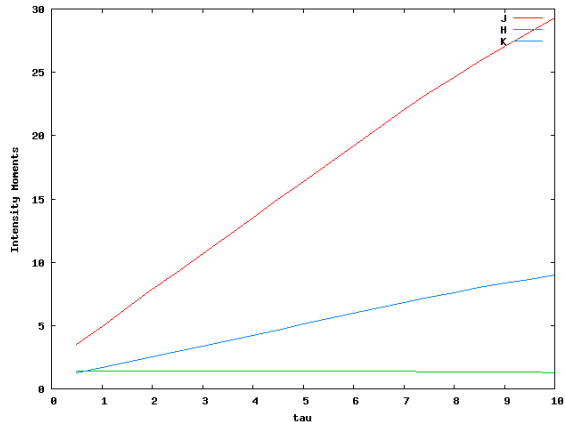


Figure 7: The discretized intensity moments after normalization by N_t ; parameters $\tau_{\max} = 10, z_{\max} = 1.0, a = 1, k = 20, N_t = 10^5$. With the exception of H (the mean flux), data for these plots includes only those transitions where $\cos \theta$ was greater than 0, ie. for which a photon moved closer to the observer’s side of the slab. The τ -axis should be read “from right to left”.

addition, each scattering event may change a photon’s polarization state, which in reality affects the observed radiant energy. Therefore a proper treatment should also include polarization effects for every photon tracked. We will next outline how each of these points can be addressed.

3.3.1 Cartesian Grid

The most straightforward improvement to the program’s ability to simulate more complex systems is to replace the semi-infinite slab by a 3D grid of cells, where each cell has the same dimensions and represents a small region of (variable) uniform density and opacity. The number of cells along each coordinate axis determines the grid’s *resolution*, while the *size* of the volume of space bounded by the edges of the grid is a direct function of cell size and resolution. This spatial partitioning scheme can

then be used to construct density distributions of any geometrical kind within the grid’s resolvable range. To step a photon through the grid, we calculate its distance to the closest cell wall along the photon’s direction of travel⁶ and move it into the corresponding neighbour grid element. The tracking stops when a photon escapes the grid confines.

At the same time, because the $n\sigma$ term of equation (11) can no longer be considered a constant, we must integrate the optical depth along the path of the photon to find each interaction location. The discretization of the medium means that, within a single cell, the optical depth τ_c along any path segment of length s can be written as $\rho_c \kappa_c s$. Thus, the integration simply amounts to sampling a random optical depth τ as before and moving a photon cell by cell until its cumulative encountered depth τ_r exceeds this value, ie. until $(\tau_r + \tau_c) > \tau$. The scattering or absorption position is then found at a distance $\frac{\tau - \tau_r}{\rho_c \kappa_c}$ into the last entered cell.

Figure 8 shows a simulation output example for a “letterbox”-shaped grid. By varying ρ_c and κ_c in every cell c , more elaborate dust configurations (such as accretion discs around young stars) can be studied as well. However, a downside of Cartesian grids is that all cells are of equal size, which makes them less suitable for the representation of systems with extreme differences in scale (eg. entire galaxies). Another disadvantage is the amount of memory required to store the cells. For these reasons, specifying the grid in spherical coordinates with logarithmically increasing cell radii is sometimes preferred.

3.3.2 Anisotropic Scattering

Dust particles have a complex influence on incident radiation that cannot adequately be simulated with isotropic scattering. Instead the scattering behavior is characterized by the Henyey-Greenstein phase

⁶Each photon maintains a pointer to the cell it currently occupies; this may initially be any cell in the grid.

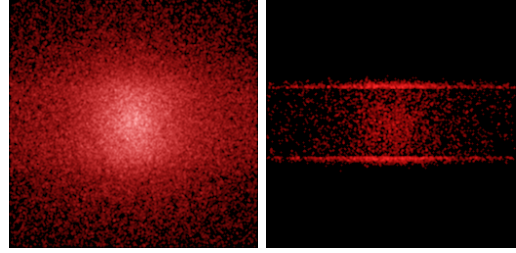


Figure 8: Isotropic scattering in a grid of spatial width 400, height 100, and depth 100 (with a resolution of 20 cells per dimension). Boundary effects are most clearly visible when projecting only photons that emerged parallel to the observer direction, which was done for the image on the right. Each cell was assigned a fixed ρ_c of $2 \cdot 10^{-1}$ and κ_c of $1 \cdot 10^{-1}$, the photon emission source ($N_t = 10^5$) was placed in the center cell.

function [11]:

$$P(\cos(\Theta), g) = \frac{1 - g^2}{4\pi(1 + g^2 - 2g \cos(\Theta))^{3/2}} \quad (13)$$

Here Θ is the directional *difference* in the photon’s *local* frame of reference and g the *scattering asymmetry* parameter, which is defined as the *mean cosine* of the scattering angle (often denoted by $\langle \cos \Theta \rangle$). This function acts isotropically for $g = 0$, but gradually becomes forward-throwing as $g \rightarrow 1$. Note also that there is no dependence on the azimuthal angles ϕ_i and ϕ_o or on the incoming radiation’s polarization state; more general formulations that do take these factors into account may be found in the literature.

The cosine of the scattering angle Θ itself is sampled from

$$\cos \Theta = \frac{1}{2g} \left[1 + g^2 - \left(\frac{1 - g^2}{1 - g + 2g\xi} \right)^2 \right] \quad (14)$$

where ξ is a random number $\in [0, 1]$. It is however crucial to realize that Θ is defined within the scat-

tering plane of the photon, whereas the photon's incoming direction angles (θ_i, ϕ_i) are defined with respect to the global Cartesian reference frame of the simulation. Setting the new outgoing (θ_o, ϕ_o) angles thus demands some trigonometry. This also plays an important role in the correct consideration of polarization effects, which is the topic of the next section. Figure 9 diagrams the relevant vectors, figure 10 the extent of the anisotropy for various values of g .

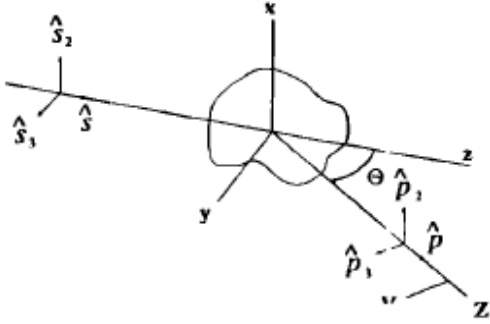


Figure 9: The Θ scattering angle. \hat{s} is the photon's local coordinate system prior to scattering, \hat{p} its system afterwards. Diagram from [12].

3.3.3 Polarization

An electromagnetic wave's polarization state is related to the (complex) amplitudes E_x and E_y of its electric field, the components of which can be decomposed into two perpendicular vectors in a plane that is orthogonal to the propagation direction of the wave. These two vectors form a basis (\hat{x}, \hat{y}) in which the two amplitudes can be expressed as a linear combination. However, a more convenient notation for dealing with non-linear states⁷ are the *Stokes parameters*

⁷A wave may have a time-varying oscillation direction where the electric-field vector traces out a circular or elliptical pattern in the plane orthogonal to the direction of travel.

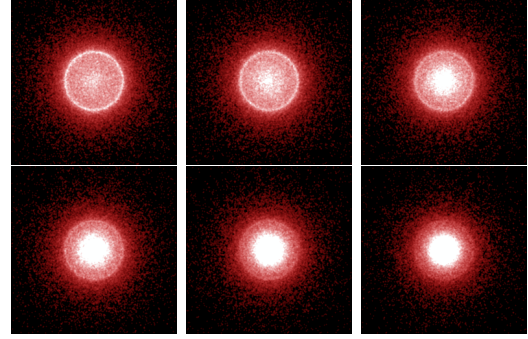


Figure 10: The effect of scattering anisotropy on the energy observed to leave the plane-parallel slab ($g \in [0.2, 0.7]$, $\rho = 1.5$, $\kappa = 2.5$, $N_t = 10^5$). For $g = 0 + \epsilon$, the output and intensity moments are similar to figures 5 and 7.

eters I , Q , U , and V , sometimes also labelled as S_0 , S_1 , S_2 , and S_3 :

$$\begin{aligned} I &= |E_x|^2 + |E_y|^2 \\ Q &= |E_x|^2 - |E_y|^2 = Ip \cos 2\psi \cos 2\chi \\ U &= |E_a|^2 - |E_b|^2 = Ip \sin 2\psi \cos 2\chi \\ V &= |E_l|^2 - |E_r|^2 = Ip \sin 2\chi \end{aligned}$$

(E_x, E_y) , (E_a, E_b) , and (E_l, E_r) are the amplitude pairs in the standard, rotated (by 45 degrees), and circular bases (\hat{x}, \hat{y}) , (\hat{a}, \hat{b}) , and (\hat{l}, \hat{r}) respectively. The I -component is the total intensity, Q and U measure the degree of linear polarization in the two Cartesian bases, and V indicates the amount of circular polarization. A more detailed discussion of these parameters is given in [6] and [13] amongst others; figures 11 and 12 show their meaning (in the geometrical sense) and some examples. Every time a photon is scattered, its polarization⁸ (and hence its Stokes parameter vector $S = (I, Q, U, V)^T$) changes via the transformation

$$S_{t+1} = L(\pi - i_2)R(\Theta)L(-i_1)S_t \quad (15)$$

⁸Photons start life unpolarized, $S = (1, 0, 0, 0)$.

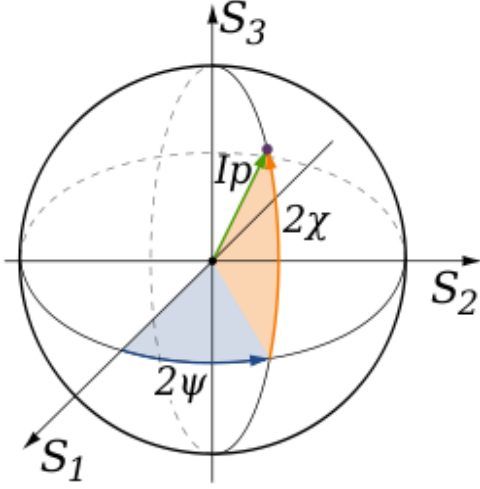


Figure 11: The geometric interpretation of the Stokes parameters in spherical coordinates 2ψ , 2χ , and Ip . The sphere's radius is I , points inside the sphere correspond to radiation that is partially polarized. Unpolarized radiation corresponds to the center of the sphere. The northern and southern hemispheres denote elliptical polarization, while the equatorial plane denotes linear polarization. The doubled angles (2ψ and 2χ) signify that polarization states are invariant under rotation by 180 degrees. Image assumed to be in the public domain.

where $L(\alpha)$ is the parameterized Mueller rotation matrix with elements

$$L(\alpha) = \begin{pmatrix} 1 & 0 & 0 & 1 \\ 0 & \cos(2\alpha) & \sin(2\alpha) & 0 \\ 0 & -\sin(2\alpha) & \cos(2\alpha) & 0 \\ 0 & 0 & 0 & 1 \end{pmatrix}$$

which transforms the Stokes vector from the meridian plane to the scattering plane and subsequently to the scattered meridian plane. $R(\Theta)$ is the sparse⁹

⁹That is, filled without regard for magnetization effects.

| 100% Q | 100% U | 100% V |
|--|--|--|
| $+Q$ $Q > 0; U = 0; V = 0$ (a) | $+U$ $Q = 0; U > 0; V = 0$ (c) | $+V$ $Q = 0; U = 0; V > 0$ (e) |
| $-Q$ $Q < 0; U = 0; V = 0$ (b) | $-U$ $Q = 0; U < 0; V = 0$ (d) | $-V$ $Q = 0; U = 0; V < 0$ (f) |

Figure 12: Degenerate polarization states. Image assumed to be in the public domain.

scattering matrix

$$R(\Theta) = \begin{pmatrix} P_1 & P_2 & 0 & 0 \\ P_2 & P_1 & 0 & 0 \\ 0 & 0 & P_3 & -P_4 \\ 0 & 0 & P_4 & P_3 \end{pmatrix}$$

that holds the scattering probability for a specific angular difference Θ in the frame of the dust particle. The elements of $R(\Theta)$ are

$$\begin{aligned} P_1 &= \frac{1 - g^2}{(1 + g^2 - 2g \cos(\Theta))^{3/2}} \\ P_2 &= -p_l \frac{1 - \cos(\Theta)^2}{1 + \cos(\Theta)^2} \\ P_3 &= P_1 \frac{2 \cos(\Theta)}{1 + \cos(\Theta)^2} \\ P_4 &= -p_c P_1 \frac{1 - \cos(\Theta_f)^2}{1 + \cos(\Theta_f)^2} \end{aligned}$$

where

$$\Theta_f = \Theta \cdot \left(1 + 3.13s \exp\left[-\frac{7\Theta}{\pi}\right] \right)$$

and the constants p_l , p_c , and s contain information about the peak linear and peak circular polarization properties of the dust medium and its skew factor. The combined transformation can be visualized as in figure 13. We can now condense

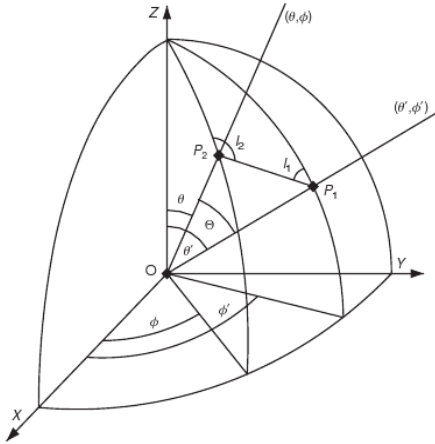


Figure 13: Geometry of the Stokes vector transformation from the incoming meridian plane OP_1Z to the outgoing meridian plane OP_2Z via the intermediate scattering plane OP_1P_2 . This image appears in various guises throughout the literature.

the whole anisotropic scattering procedure into four parts:

- Sample i_1 from $2\pi\xi$, $\xi \in [0, 1]$. This is the angle that plays the part of ϕ in the photon's local reference frame.
- Sample Θ from equation (14), transform it to the global reference frame and calculate the photon's new θ and ϕ angles based on its transformed value.
- Compose the scattering matrix $R(\Theta)$ from the – untransformed – Θ and the rotation matrix $L(-i_1)$; calculate i_2 (a direct expression for this angle is provided in eg. [13] and [7]) and compose the matrix $L(\pi - i_2)$.
- Update S in accordance with equation (15); normalize the new vector such that $I = 1$.

Upon projection of a photon onto the image plane, its final polarization state can be recorded so that

we may inspect the Q , U , and V images of the observed emergent radiation. Time unfortunately did not permit us to implement this.

4 Parallelization

Monte Carlo radiative transfer simulations following a design as sketched out in the previous sections have three main execution bottlenecks. For one, the size and resolution of the grid directly contribute to the time it takes for photons to complete their random walks through the medium. Also, with higher optical depth, interaction events happen more frequently, further adding to the travel time. Finally, the amount of photons released acts as a multiplier for these terms, but must be large in order to obtain a good signal-to-noise ratio in the output data. The only way¹⁰ we can offset this is by distributing the computational load, either over multiple *threads* of execution or over multiple *processes* (most commonly by clustering separate physical machines). This is possible because every photon path is an independent Markov chain, so each thread or process may draw its own share of samples (photons) from the parameter space. Furthermore, no thread or process needs to communicate with another except to merge individual results when all are finished¹¹. The absence of communication overhead means a near-linear speedup is achievable with each extra thread or process spawned. Our implementation only employs threads, but could be modified to also support the MPI clustered-computing protocol with little effort. Figure 14 conveys the effectiveness of parallelizing at the thread level.

¹⁰Juvela [8] describes four importance weighting methods to more efficiently sample the radiation field for a given photon count, but their benefit is highly model-dependent.

¹¹The grid itself is not decomposed; each processing subtask operates on all cells.

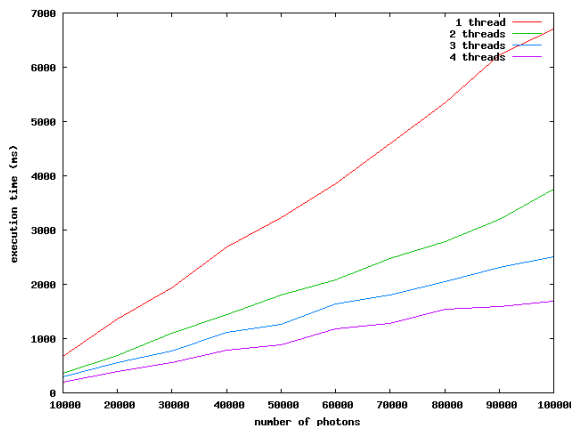


Figure 14: Execution times of runs of $N_t = 10^5$ photons (in an isotropic scattering environment) with 1 to 4 active threads on a quad-core CPU.

5 Conclusion

Due to external factors, we could not perform as many experiments (in particular, one to study a replica of the Pleiades star cluster) with the simulation as desired. We also could not afford a more thorough analysis of the current state of the art in Monte Carlo (eg. STOKES [10], or MC3D [9]) or other radiative transfer models, such as those listed in [3]. Nevertheless we have gained valuable insight into many of the issues surrounding the simulation of the RT problem and became familiar with at least one important application, although (in terms of mathematical depth) this only scratches the surface. In its present condition the program written to accompany this report will likely not meet the demands of astronomical research, but may be sufficient for modelling elementary dust configurations and can serve as an introduction to implementing a more capable Monte Carlo radiative transfer simulation in its own right.

References

- [1] K. Wood, B. Whitney, J. Bjorkman, and M. Wolff: *Introduction to Monte Carlo Radiation Transfer* (2001)
- [2] S. Chandrasekhar: *Radiative Transfer* (1960)
- [3] N. D. Kylafis and E. M. Xilouris: *Radiation Transfer Models in Galaxies* (2005)
- [4] N. Metropolis: *The Beginning of the Monte Carlo Method* (1987)
- [5] K. D. Gordon, K. A. Misselt, A. N. Witt, and G. C. Clayton: *The DIRTY Model (I): Monte Carlo Radiative Transfer Through Dust* (2000)
- [6] Hulst, H. C. van de: *Light Scattering by Small Particles* (1981)
- [7] L. Margerin: *Introduction to Radiative Transfer of Seismic Waves* (2003)
- [8] M. Juvela: *Efficient Monte Carlo Methods for Continuum Radiative Transfer* (2005)
- [9] S. Wolf: *MC3D - 3D Continuum Radiative Transfer (Version 2)* (2002)
- [10] R. Goosmann: *The Radiative Transfer Code STOKES (Version 1)* (2004)
- [11] L. Henyey and J. Greenstein: *Diffuse Radiation in the Galaxy* (1941)
- [12] J. Turner and R. Weaver: *Radiative Transfer and Multiple Scattering of Diffuse Ultrasound in Polycrystalline Media* (1993)
- [13] M. Drusch and S. Crewell: *Principles of Radiative Transfer* (2002)